Microscale laser peen forming of single crystal

Youneng Wang,[a] Yajun Fan, Jeffrey W. Kysar, Sinisa Vukelic, and Y. Lawrence Yao
Department of Mechanical Engineering, Columbia University, New York, New York 10027, USA

(Received 15 August 2007; accepted 10 January 2008; published online 28 March 2008)

As the result of quickly increased requirement in many industrial products resulting from microtechnology, laser thermal microforming and microsurface treatment [microscale laser shock peening (μLSP)] have been well studied. By combining the beneficial effects of these two processes with a controlled bending deformation, microscale laser peen forming (μLPF) attracts more attention recently since it not only improves the fatigue life of the material but also shapes microscale metallic parts at the same time. In the present study, μLSP of single crystal aluminum was presented to study anisotropic material response. Local plastic deformation was characterized by lattice rotation measured through electron backscatter diffraction. Residual stress distributions of both sides of a peened sample, characterized by x-ray microdiffraction, were compared with the results obtained from finite element method simulation. μLPF anisotropic behavior was investigated in three effective slip systems via both the anisotropic slip line theory and numerical method. Also, the work hardening effect resulted from self-hardening, and latent hardening was analyzed through comparing the results with and without considering hardening. © *2008 American Institute of Physics*. [DOI: 10.1063/1.2891573]

I. INTRODUCTION

It is well known that laser shock peening (LSP) can induce desirable compressive residual stresses in the target and improve its fatigue life.[1,2] Recently, a forming technology known as laser peen forming (LPF) which is developed from LSP has attracted more attention because of the inherent advantage of LPF. It is undesirable to form large structural components by bending or hydraulic pressing since these processes result in tensile residual stress on surfaces subject to fatigue and stress corrosion cracking. As a result, mechanical shot peen forming was developed and has been used for over 40 years to shape many of these large components. LPF now can compliment this traditional forming technology and has much greater depth of residual stress, which results in three to eight times greater curvature than can be achieved with mechanical shot peen forming.[3] Also, compared with shot peen forming, a desired shape may be achieved by LPF with more accuracy and better repeatability, and faster.

Hackel and Harris[4] employed a pulse laser beam of an energy fluence of 60–200 J/cm^2 with a spot size ranging from 3×3 to 6×6 mm^2 for forming shapes and contours in metal strips. They showed that the LPF process can generate deep compressive stress without inducing unwanted tensile stress at the metal surface and is especially useful for thick (greater than $\frac{3}{4}$ in. thick) material that is difficult to shape or contour. Zhou *et al.*[5] investigated the deformation mechanisms for a special configuration; that is, a sample clamped by two concentric washers. Laser spot size they used ranges from 3 to 10 mm in diameter. By using LPF, metal sheet forming is realized without mold and the dimensions of the obtained shapes are determined by the boundary condition. Zhou *et al.*[6] further studied response of various metal sheets to LPF and presented detailed deformation characterization. The investigation showed its potential to become a flexible manufacturing process with excellent properties and short manufacturing time.

Recently, microforming becomes a more important technology to manufacture micrometallic parts, in particular, for bulk production, because of quickly increased requirement in many industrial products resulting from microtechnology.[7,8] Microforming using laser has already been explored for a number of potential high-precision industrial applications, such as laser microbending of magnetic disk-drive components, adjustment of contact springs of miniature relays and reed contacts, accurate bending of thin plate springs, etc.[9,10] It can be seen that most of these applications encounter cyclic loadings. Thus, it is desirable to improve fatigue life of microparts after microforming process.

Microscale laser peen forming (μLPF) has already attracted some attentions.[11] They showed that compressive stresses, like in the macro-LPF process, can also be induced at the surface of both sides by microscale LPF. However, an important consideration in understanding the mechanics of μLPF at the microscale is that the laser spot size is likely to be in the same order of magnitude as the average grain size of the target so that the deformation is expected to occur predominately within a small number of grains. Thus in order to accurately model the process, the material properties must be treated as anisotropic and heterogeneous rather than isotropic and homogeneous. In order to gain insight into the deformation and stress fields associated with μLPF, it is advantageous to apply the process to single crystal so that the effects of the anisotropy can be identified in a homogeneous material.

In this paper, the effects of microscale LPF on single crystal aluminum are studied by using both numerical and experimental methods. Beside residual stress distribution measured by x-ray microdiffraction, peen formed crystal

[a]Electronic mail: yw2119@columbia.edu.

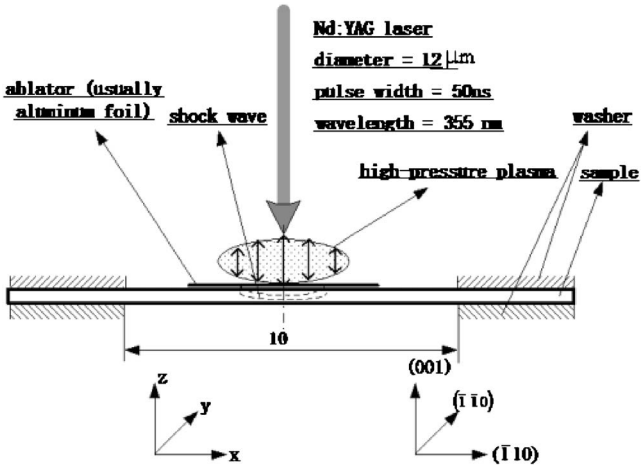

FIG. 1. Sample geometry and LPF condition.

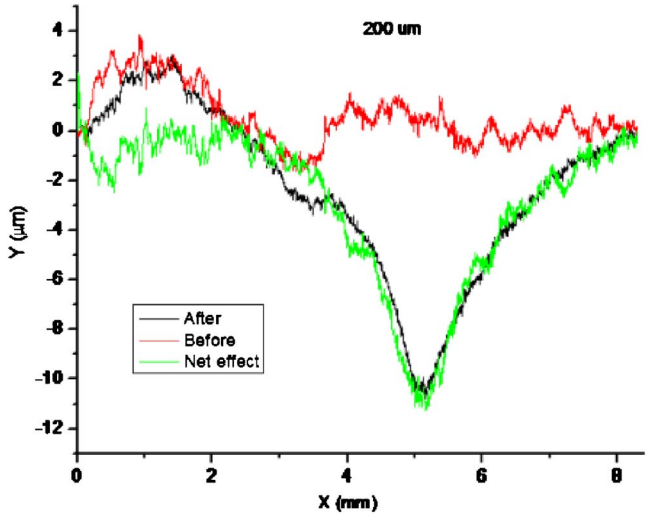

FIG. 2. (Color online) Curvature measurement on the bottom side before and after peen forming for 200 μm sample with 3.57 GW/cm^2 laser intensity.

samples are also characterized by profilometer curvature measurement and lattice rotation of electron backscatter diffraction (EBSD). In addition, a preliminary numerical simulation based on single crystal plasticity was presented to understand the process of μLPF, especially anisotropy and effect of strain hardening. Anisotropic slip line theory was employed to compliment the numerical simulation to explain the stress and deformation state resulting from LPF on a single crystal surface under plane strain conditions. Through the presented work, we can grab some main features of microscale peen forming and shed some shine for future work on understanding heterogeneity and associated problems of the ultrahigh strain rate plastic deformation related to laser shocking.

II. EXPERIMENTAL CONDITIONS

A frequency tripled *Q*-switched Nd:YAG laser (λ =355 nm) in TEM$_{00}$ mode was used in microscale LPF and the parameters of pulse duration (50 ns), wavelength (355 nm) and beam diameter (12 μm) are shown in Fig. 1. If a line loading is applied parallel to a $\langle 110 \rangle$ direction in a fcc crystal, certain slip systems act cooperatively which enable approximate plane strain deformation conditions to be achieved.[12] Therefore, a line of μLSP shocks parallel to a $\langle 110 \rangle$ direction was created on the sample surface with a 25 μm spacing because this spacing results in approximate two-dimensional deformation. Pulse energies, 202 and 280 μJ, corresponding to laser intensities of 3.57 and 4.95 GW/cm^2, respectively, were applied. A thin layer of high vacuum grease (about 10 μm thick) was spread evenly on the sample surface to isolate the thermal effect from the coating, and a 16 μm thick polycrystalline aluminum foil, chosen for its relatively low threshold of vaporization, was tightly pressed onto the grease. The sample was placed in a shallow container filled with distilled water around 1 mm above the sample's top surface to confine the produced plasma. The induced deformation is due to shock pressure and not due to thermal effects since only the coating is vaporized during the process.[2]

In order to investigate the effects of specimen thickness under the same laser energy, the samples of single crystal aluminum with 150, 200, and 300 μm thicknesses have been chosen, which have normal orientation of (001), as shown in Fig. 1. The samples were cut to the dimension of 20 $\times$3 mm^2 by using wire electrical discharge machining (EDM) and mounted to holders as shown in Fig. 1 carefully to make them as flat as possible. The sample surface on both sides was polished mechanically, in order to remove the thermal affected layer by EDM, and then electropolished to eliminate residual stress. Before shocking process, the prebending is measured by using a Mitutoyo SJ-201P profilometer as shown in Fig. 2, and the samples with a prebending less than $\pm$2 μm were chosen to minimize the prebending effects.

III. POSTPEEN FORMING MATERIAL CHARACTERIZATION

After LPF, the sample was characterized by curvature change, residual stress distribution, and lattice rotation. The characterization of curvature change is necessary for studying capability of microscale curvature adjustment by μLPF and second for its potential to improve fatigue life. Lattice rotation, accounting for the rotation part in the polar decomposition of elastic deformation, is induced by plasticity and can be quantitative analyzed by EBSD. Thus, we can directly compare the experimental results of lattice rotation with simulation results.

The curvature change is characterized by using profilometer measurement, whose range in depth direction is 350 μm with the resolution of 0.4 μm. The measuring force is 4 mN, which assures that the detector has no bending effect on the samples while measuring. Significant effort has been put to manually polish specimens such that curvature prior to shocking is about $\pm$2 μm. Moreover deformation after shocking is about 10 μm, as seen on Figs. 2 and 3, and it will be discussed in detail in following section. Residual stresses were estimated from x-ray microdiffraction profiles, which were collected from Beamline X20A (synchrotron radiation sources) at National Synchrotron Light Source at

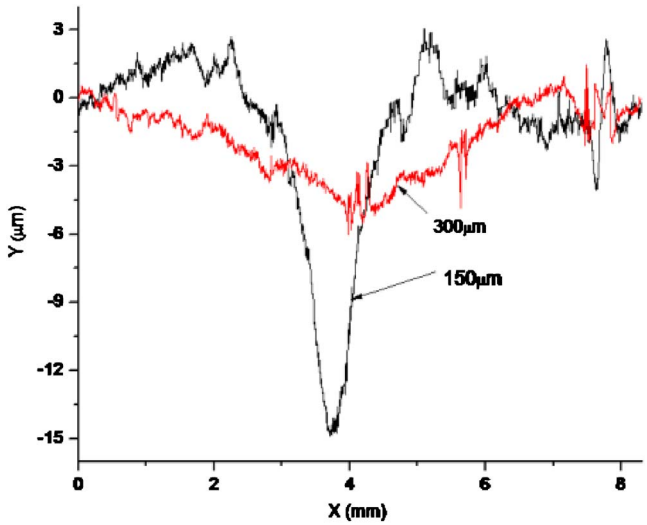

FIG. 3. (Color online) Curvature measurement for 150 and 300 μm sample with low energy.

Brookhaven National Laboratory. X ray of X20A can be focused by a tapered glass capillary to spot sizes as small as 3 μm. Complete details of x-ray microdiffraction experiment and the corresponding evaluation method of subprofile analysis can be found in Chen *et al.*[13] For lattice rotation, the crystallographic orientation of peened area for both top and bottom surfaces was collected using EBSD, which provided information about the lattice rotation on the shocked area. EBSD data were collected using a system supplied by HKL Technology and attached to a JEOL JSM 5600LV scanning electron microscope.

IV. FINITE ELEMENT METHOD (FEM) SIMULATION CONDITIONS

In this section, we present results of elementary FEM simulations of microscale LPF. Since the surface deformation and lattice rotation under LSP indicate that an approximate two-dimensional deformation state exists, we will assume that the induced deformation state is strictly two dimensional, which may be a gross oversimplification. However, it turns out that such an approach can shed significant insight into the mechanics of deformation which will be useful when the full three-dimensional problem is addressed in future studies. Simulations of LPF pose many significant challenges because of the high transient pressures, fluid-solid interaction, and high strain rates in single crystal at the micrometer length scale. Given the absence of constitutive data in this region, it is impossible to incorporate realistically these effects into the model. Hence, we will make a grossly simplified assumption of ideal plastic behavior under quasistatic plane strain conditions with hardening as seen below. Rate effects and three-dimensional effects are neglected.

Finite element simulations based on single crystal plasticity[14] were carried out with a user-material subroutine (UMAT), which was written by Huang[15] and modified by Kysar.[16] It is incorporated into the finite element analysis using the general purpose finite element program ABAQUS/Standard. In the UMAT, the $\{111\}\langle 110\rangle$ slip systems in fcc metal are employed and a critical resolved shear strength $\tau_{\mathrm{CRSS}} \approx 1$ MPa is assumed for each of the slip systems. The element used in the simulation was a plane strain reduced integration, hybrid element (CPE4RH) and total simulation size is 384×192 μm^2 (thickness $\times$ width). The mesh size is about 0.1 μm in the area close to the loading and 1.5 μm far away from the loading. As for boundary conditions of the plane strain model, the applied surface tractions correspond to the applied pressure on the shocked surface. At the bottom surface, the vertical displacement is specified to be zero and the outer edges are traction-free. In the simulation, elastic-ideally plastic behavior is assumed. The simulation ignores rate and inertial effects. The loading on the surface has a Gaussian distribution: $P(x)=P_0 \exp(-x^2/2R^2)$, where x is the radial distance from the center of the laser beam and R is the radius of plasma. Following Zhang and Yao,[17] the resulting plasma radius is $R=9.5$ μm at the end of the laser pulse for the laser beam diameter of 12 μm. The plasma is expected to expand further after 50 ns, but the resulting pressure decreases very quickly so that effect is ignored.[2,17] The simulation is divided into two steps, loading and relaxation step, and the maximum magnitude of applied pressure is determined by trial and error method. The pressure magnitude was varied until the simulation result of curvature change matched experimental findings. Rate dependence used is a power-law relationship proposed by Hutchinson[18] and described by Connolly and McHugh,[19] Huang,[15] Kysar,[20] Peirce *et al.*,[21] and Savage *et al.*:[22]

$$\dot{\gamma}_k = \dot{\gamma}_0 \, \mathrm{sgn}(\tau_k) \left\{ \left| \frac{\tau_k}{g_k} \right| \right\}^m, \tag{1}$$

where is $\dot{\gamma}_0$ the reference strain rate, τ_k is the applied resolved shear stress, m is the rate sensitivity exponent, and g_k is related to critical resolved shear stress of the kth-slip system, as given by Peirce *et al.*[21] In this simulation, $\dot{\gamma}_0 = 10^{-3}$ and $m=50$.

V. FEM SIMULATION CONSIDERING WORK HARDENING

In LPF, the target is subjected to very strong shock pressures (>1 GPa), the interaction time is very short (<100 ns), and the strain rate is very high (>100 000 s^{-1}). A review of the constitutive equations for such high strain rates was given by Meyer.[23] The simplest model to describe the work hardening behavior of metals is Ludwik equation: $Y = A + B\varepsilon^n$ at ambient temperature and quasistatic loading, where Y is the yield strength, n, A, and B are material constants, and ε is the equivalent plastic strain. For single crystals of face-centered-cubic (fcc) metals, work hardening experiences three stages.[24] During stage I, dislocations move on a single set of parallel slip planes and there is little work hardening. Stage II hardening starts when intersecting slip systems are activated and dislocations moving on the intersecting glide planes entangle each other. Dislocation density increases rapidly with increasing strain in stage II. At higher strains, stage III happens when the rate of work hardening diminishes with increasing strain because screw dislocations can cross slip from one slip plane to another and so bypass obstacles and annihilate dislocations of opposite sign in

neighboring planes at sufficiently high stresses. For most polycrystalline cubic metals, stage III work hardening is the dominant mode observed in tests on most at room temperature. Because approximately linear stage II hardening may be present in the early stages of straining, Ludwik equation is often poor at low strains for fcc single crystals of metals.

In this paper, Asaro's hardening theory of single crystal[14] has been applied, in which the critical shear stress τ_0^k of the Schmid law is determined by the current dislocation density and substructure and represents variation of hardness of material due to work hardening. Since work hardening of slip system depends on shear deformation of slip systems, variation of τ_0^k may be estimated by

$$\Delta\tau_0^k = h_1^k|\Delta\gamma_1| + h_2^k|\Delta\gamma_2| + h_3^k|\Delta\gamma_3| + h_4^k|\Delta\gamma_4| + \cdots = \sum_i h_i^k|\Delta\gamma_i| \tag{2}$$

or

$$\begin{Bmatrix} \Delta\tau_0^1 \\ \Delta\tau_0^2 \\ \Delta\tau_0^3 \\ \vdots \\ \Delta\tau_0^{12} \end{Bmatrix} = \begin{bmatrix} h_1^1 & h_2^1 & h_3^1 & \cdots & h_{12}^1 \\ h_1^2 & h_2^2 & h_3^2 & \cdots & h_{12}^2 \\ h_1^3 & h_2^3 & h_3^3 & & \vdots \\ \vdots & \vdots & & \ddots & h_{12}^{11} \\ h_1^{12} & h_2^{12} & \cdots & h_{11}^{12} & h_{12}^{12} \end{bmatrix} \begin{Bmatrix} |\Delta\gamma_1| \\ |\Delta\gamma_2| \\ |\Delta\gamma_3| \\ \\ |\Delta\gamma_{12}| \end{Bmatrix}, \tag{3}$$

$$\{\Delta\tau_0\} = [h]\{|\Delta\gamma|\}, \tag{4}$$

where h_i^k expresses hardening rate against increment of shear deformation $\Delta\gamma_i$ on each slip system. When k equals to i, h_i^k represents hardening by glide on its own slip system. When k is not the same as i, h_i^k represents hardening by glide on other slip systems. The former is called the self-hardening, and the latter is called the latent hardening. It is found that latent hardening rate does not depend on combination of slip systems. The ratio denoted by q between latent hardening rate and self-hardening rate can be evaluated by the following equation:[14]

$$h_i^k = qh + (1-q)h\delta_{ij} = h\begin{bmatrix} 1 & q & q & \cdots & q \\ q & 1 & q & \cdots & q \\ q & q & 1 & & \vdots \\ \vdots & \vdots & & \ddots & q \\ q & q & \cdots & q & 1 \end{bmatrix} \tag{5}$$

and $q=1.4$ is best to match simulation with experimental results. Where h is given by

$$h = h_0 \operatorname{sech}^2\left(\frac{h_0\gamma}{\tau_{\max}^k - \tau_0^k}\right), \tag{6}$$

$$\gamma = \sum_i |\Delta\gamma_i|, \tag{7}$$

where $\tau_{\max}^k$ is the maximum value of yield shear stress, τ_0^k is the initial value of yield shear stress, and h_0 is a material constant. In this paper, $h_0=8.9\tau_0$ and $\tau_{\max}^k=1.8\tau_0$ are used.[14]

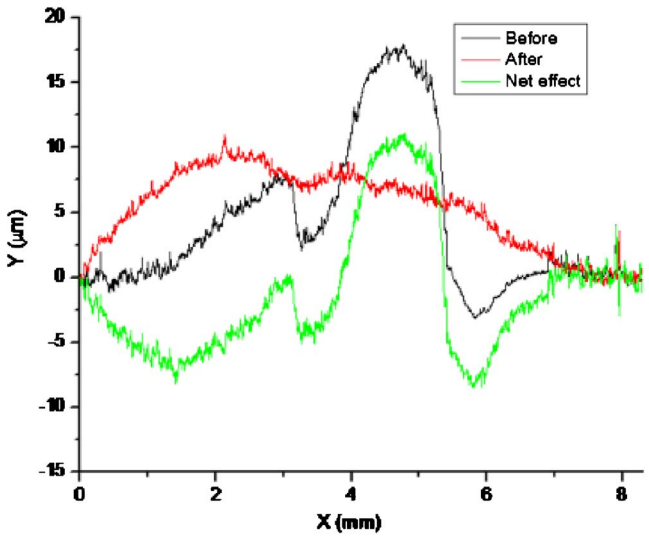

FIG. 4. (Color online) Curvature measurement for 150 μm with high energy.

VI. RESULTS AND DISCUSSION

A. Curvature changes

Our previous work[11] showed that 100 μm thick polycopper with 3.57 GW/cm^2 laser intensity was bent downward, while the same sample was bent upward with high laser intensity of 4.95 GW/cm^2. In this paper, in order to verify the deformation mechanism of LPF, these two levels of laser intensity were used for single crystal aluminum as well, but the minimum thickness of 150 μm rather than 100 μm was selected because single crystal aluminum is much softer than polycopper. For the aluminum single crystal, as it can be seen in Figs. 3 and 4, 150 μm thick sample was bent downward with low laser energy of 3.57 GW/cm^2 intensity and bent upward with high laser energy of 4.95 GW/cm^2 intensity. This trend is consistent with the case of polycopper samples and detailed explanation can be found in our previous work.[11] In order to examine thickness effects, we have also applied laser shocks (3.57 GW/cm^2 intensity) onto specimens with different thicknesses. The curvature changes of 200 μm sample in Fig. 2 and 300 μm sample in Fig. 3, respectively, indicate that the curvature change decreases with thickness increases.

B. Residual stress distribution

In order to spatially resolve the residual stress induced by μLPF, measurements were made on both top and bottom surfaces along the lines perpendicular to the peened line. The spacing between the adjacent measurement points is 10 μm and the corresponding x-ray diffraction profile at each position is recorded and repeated for each scan line. Figure 5 shows the residual stress distribution for 200 μm sample with 3.57 GW/cm^2 laser intensity. It can be seen that a compressive residual stress has been generated near the center of the bottom side of the peened region and there is a tensile residual stress near the center bordered by a region of compressive stress on the top side. Although the laser spot size is only 12 μm, the high shock pressure in μLPF can generate

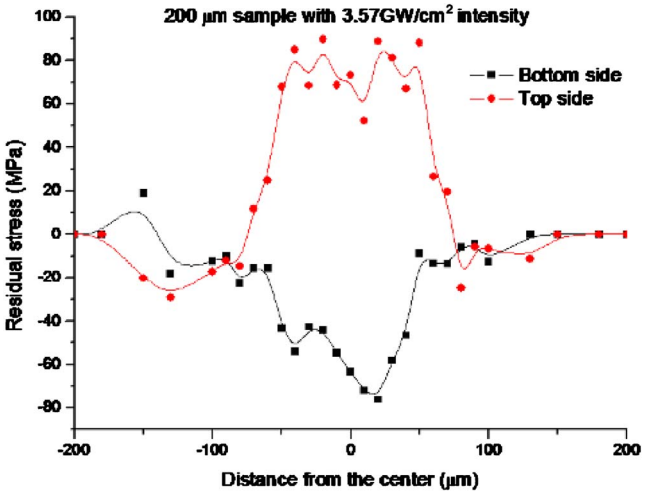

FIG. 5. (Color online) Residual stress distribution by x-ray microdiffraction for 200 μm sample.

significant compressive residual stresses over a much larger region, up to 200 μm. Figure 6 shows the residual stress distributions for 150 μm samples with two laser energy levels. Measurements indicate that high laser energy of 4.95 GW/cm^2 intensity induces compressive residual stress in both sides and the pattern with low energy of 3.57 GW/cm^2 is the same as the one of 200 μm. Similar to the results of previous work,[11] the pattern of residual stress is determined by the deformation mechanism; that is, residual stresses are compressive on both sides for upward bending while tensile on the top and compressive on the bottom for downward bending.

Figure 7 shows the simulation results of residual stress contour for 200 μm sample with 3.57 GW/cm^2 laser intensity. Residual stress patterns for the case when we observe downward bending are in good agreement with the experimental results for different thicknesses. However, for upward bending case of 150 μm thick specimen under laser intensity of 4.95 GW/cm^2, the simulation model is limited to grab the corresponding curvature change because of quasistatic loading.

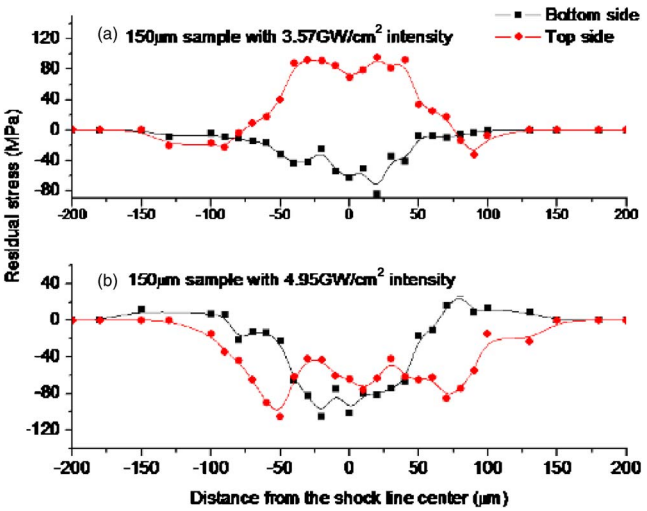

FIG. 6. (Color online) Residual stress distribution by x-ray microdiffraction for 150 μm with two laser energy levels.

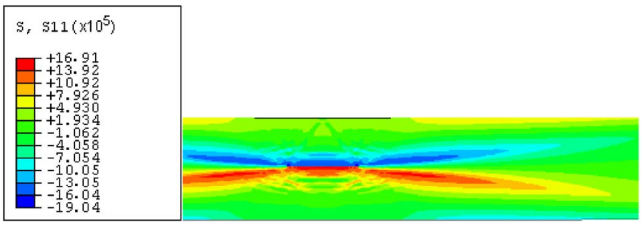

FIG. 7. (Color online) Residual stress contour by FEM simulation.

C. Lattice rotation field by EBSD

All EBSD data were acquired in the automatic mode, using external beam scanning and employing a 3 μm step size. The scan area is about 350×150 μm^2 on the shocked region, as shown in Figs. 8(a) and 8(b), respectively. The EBSD results from each individual scan comprise data containing the position coordinates and the three Euler angles which describe the orientation of the particular interaction volume relative to the orientation of the specimen in the scanning electron microscope, allowing the in-plane and the out-of-plane lattice rotations to be calculated relative to the known undeformed crystallographic orientation, which serves as the reference state. More details about this measurement technique can be found in Refs. 20 and 25.

The lattice rotation contour map of bottom surface is shown in Fig. 8(a) for 200 μm sample. Figure 8(b) shows the lattice rotation contour map for the top side. The red region corresponds to counterclockwise rotation about the y-axis (as defined in Fig. 1) which is positive and the blue region corresponds to clockwise rotation which is negative. Similar to μLSP process, the lattice rotation on top surface caused by μLPF is zero (green region) in the region far away from the shocked line which corresponds to the shock-free region. The lattice rotation distribution along the shocked line is quite uniform which suggests the approximate two-

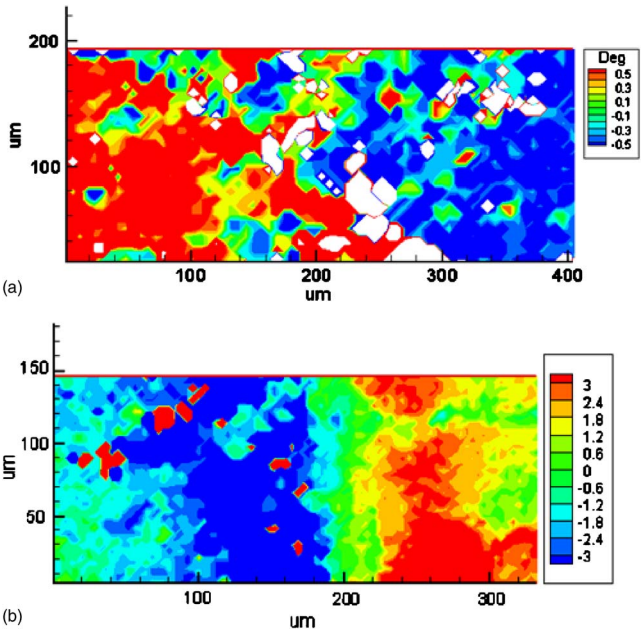

FIG. 8. (Color online) Lattice rotation distribution by EBSD measurement for 200 μm sample with 3.57 GW/cm^2 laser intensity: (a) bottom side; (b) top side.

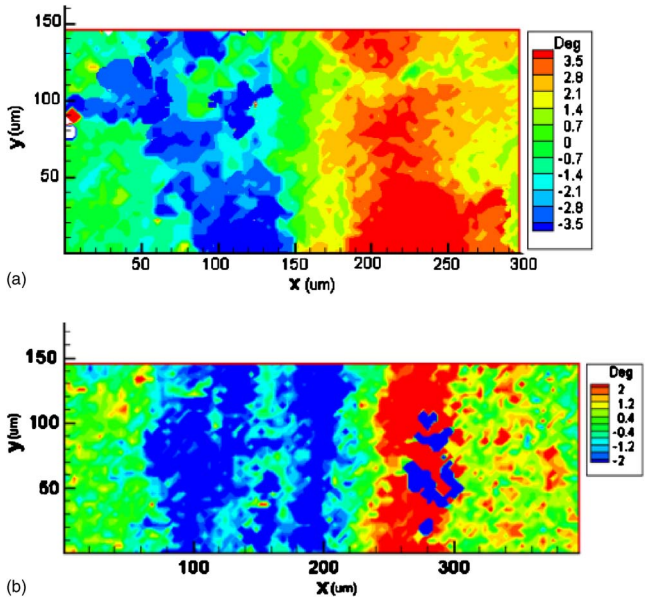

FIG. 9. (Color online) Lattice rotation by EBSD for 150 and 300 μm sample top side with low energy: (a) 150 μm; (b) 300 μm.

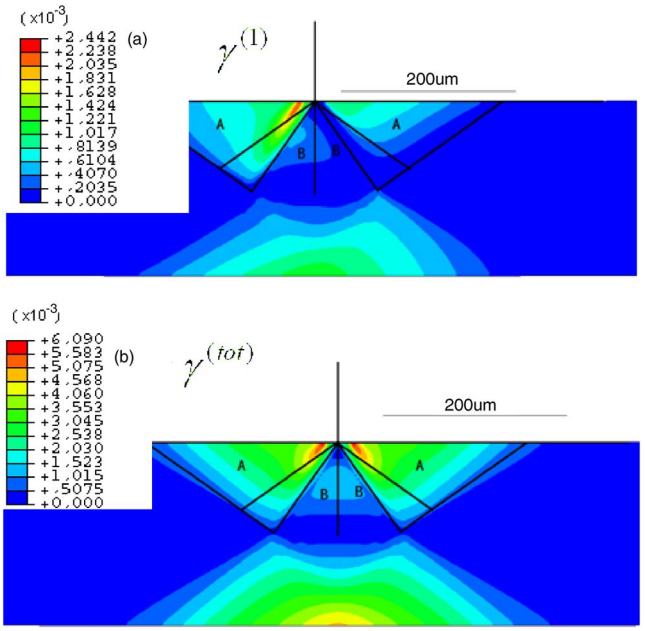

FIG. 10. (Color online) Shear strain contour in slip system: (a) slip system i; (b) total shear strain.

dimensional deformation state mentioned before. The lattice rotation value on the top surface is up to $\pm 3°$ between ± 120 μm from the center of the shocked line and the rotation direction is antisymmetric about the shock line on both sides. The rotation contour of bottom side approximately corresponds to the bending curvature since the lattice rotation in each side of shock line is almost constant and rotation value is close to the bending angle. The difference is because that the bending angle measured by profilometer reflects overall curvature while lattice rotation represents the local deformation close to the shock line.

Figure 9 presents the lattice rotation contours for 150 and 300 μm samples' top surface with low energy of 3.57 GW/cm^2. They showed similar patterns as that of 200 μm sample, but the maximum angle of lattice rotation is different and affected by the thickness. Maximum rotation angle decreases with the thickness increases, for example, 3.5° for 150 μm, 3° for 200 μm, and 2° for 300 μm sample, because of harder bending for thicker sample. Both, Figs. 8 and 9 show that deformation along the shock line is fairly uniform which indicates that approximate plane strain deformation is achieved.

D. Shear strain distribution in each slip system

Figure 10 shows the shear strain distributions for the three slip systems as well as the total shear strain by FEM simulation without considering work hardening; that is, Fig. 10(a) shows the shear strain distribution caused by slip system i, and Fig. 10(b) is for the total shear strain. The shear strain distribution of slip system iii is symmetric with that of slip system i. Because of zero Schmid's factor for slip system ii, its resulting shear strain is almost zero and is not included in Fig. 10. As seen in Fig. 10, the shear strains resulting from μLPF have certain distributional patterns. It is of great interest to understand the logics behind these patterns. In this paper, anisotropic slip line theory is applied to preliminarily explain these distributions.

According to the anisotropic slip line theory,[12,20,26] when loading is applied along the (110) direction in fcc crystals, three out of 12 slip systems will be activated. Rice[26] employed anisotropic slip line theory to solve punch problem. Wang *et al.*[27] extended this work to the μLSP, where laser induced Gaussian pressure loading is approximated as punch with nonuniform pressure distribution. Furthermore in μLSP domain of interest is considered to be semi-infinite and deformation is local. On the other hand in μLPF nature of deformation mechanism is different and global deformation has to be taken into account. Width of Gaussian pressure loading is order of magnitude smaller than width of specimen, and effect of finite geometry has to be taken into account. In order to geometrically construct a slip line field, at first similar approach as in μLSP has been taken. End points of the punch represent singular points.[28] However, from numerical simulation it appears that from perspective of global deformation, Gaussian pressure loading in μLPF more appears as a point load. It further resembles that loading can be seen as the point of singularity in which centered fan is placed. Suggested slip line field geometrically constructed this way is depicted in Fig. 11. Shear strain in top half plane should appear only in the area enclosed by $Q_1Q_4Q_7O$. Figure 10(b) shows numerical results of the total shear strain with slip line field superimposed for the comparison purposes. From Fig. 10(b) it can be seen that shear strain occurs only within the area inside of the stress sectors. Furthermore, slip system i is active in sectors, enclosed by $Q_1Q_2OQ_1$, OQ_2Q_3O, OQ_3Q_4O, and OQ_6Q_7O as shown in Fig. 11. Again, after superposition of slip sectors and numerical results [Fig. 10(a)] we see that the numerical solution of shear strain distribution for slip system i agrees fairly well with the proposed explanation. However, this issue requires further

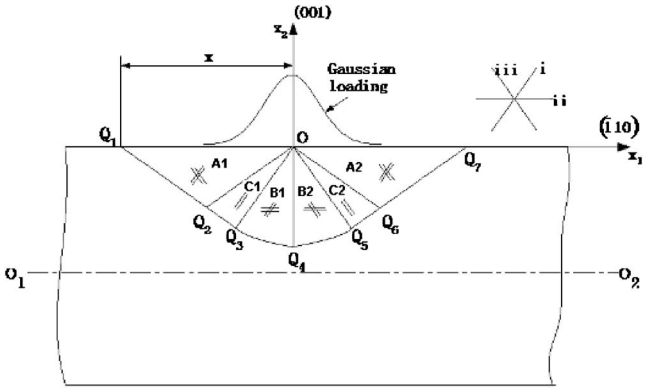

FIG. 11. Geometry of slip line field for a Guassian distribution of peen forming.

attention, more detailed analytical study of stress field based on the anisotropic slip line theory is required, which would lead to closed form solution of this problem as well as explanation of the strain behavior in the bottom half plane.

E. Effects of work hardening

In order to lay some ground for future realistic numerical simulation, which account for the material behavior under high dynamic loading with extreme high strain rate (10^7–10^9 s^{-1}) including both work hardening and strain rate effects on LPF, here we only consider the effects of work hardening to simplify the problem.

As expected, the target is hard to be deformed when encountering effects of work hardening. Figure 12 shows the difference of the bending curvatures for the single crystal aluminum sample with and without considering work hardening for the same simulation condition. The maximum displacement with work hardening consideration is around 7 μm and without work hardening is about 10 μm. For work hardening effects on total shear strain corresponding to Fig. 10(b), it is found that work hardening almost has no effect on the plastic deformation width under the previously defined simulation conditions, but the maximum of total shear strain

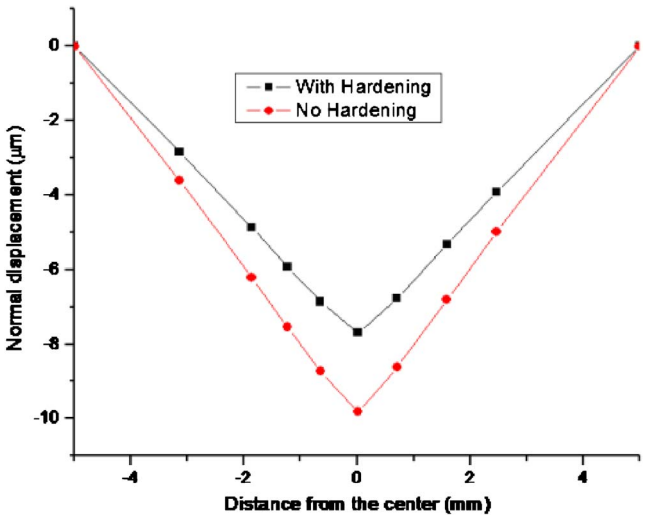

FIG. 12. (Color online) Normal displacements of FEM simulation with and without work hardening.

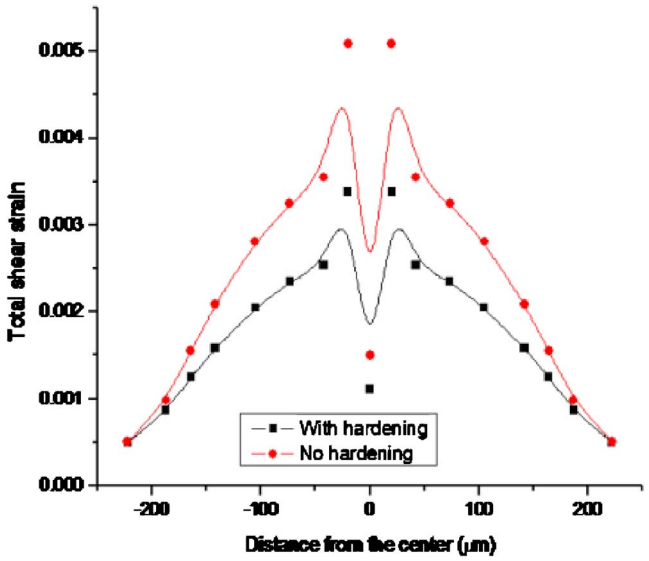

FIG. 13. (Color online) Total shear strain contour of FEM simulation with work hardening.

on the top surface is reduced almost 40% if work hardening is considered, as shown in Fig. 13. In addition, it is of great interest to look into shear strain distribution in each slip system with work hardening effects because anisotropic character associated with microscale LPF is observed in FEM simulation results under quasistatic loading without considering work hardening and high strain rate effects. Comparing simulation results of shear strain distribution in each slip system without and with work hardening, it is found that the patterns and effected area are same for these two conditions. Therefore, we have more confidence that this anisotropy is more likely associated with μLPF, but the magnitude of shear strain will become smaller if considering high strain rate effects.

VII. CONCLUSION

In this paper, μLPF of single crystal aluminum with orientation [001] under approximate plane strain condition was investigated using both experimental and numerical methods. Construction of the slip line field is proposed. Like μLSP, it was found that the potential exists for rapid changes in field variables for μLPF as well. The lattice rotation field under LPF is found to be antisymmetric on both top and bottom surfaces and top side is similar to μLSP, but bottom side proximately accounts for the curvature slope of global deformation. The magnitude of lattice rotation on the top surface increases with sample thickness decreases, such as $\pm 2°$ for 300 μm, $\pm 3°$ for 200 μm, and $\pm 3.5°$ for 150 μm, and lattice rotation covers a region around ± 150 μm across the shock line. Comparing with previous work of μLPF on the polycrystalline copper, it was found that anisotropy has little effect on bending mechanisms. Similarly, residual stresses are compressive on bottom side for both upward and downward bendings of single crystals and are tensile on top side for downward bending and compressive for upward bending. The methodologies and results presented herein enable a sys-

tematic study of the microscale LPF process and shed some light on understanding LPF process under microscale length.

ACKNOWLEDGMENTS

This work is supported by the National Science Foundation under Grant Nos. DMI-02-00334 and DMI-06-20741. J.W.K. would like acknowledge support by the National Science Foundation under the Faculty Early Career Development (CAREER) Program with Grant No. CMS-0134226. Single crystal sample preparation provided by Dr. Yongxue Gang is also acknowledged.

[1]A. H. Clauer and J. H. Holbrook, *Shock Waves and High Strain Phenomena in Metals-Concepts and Applications* (Plenum, New York, 1981), p. 675.
[2]W. Zhang and Y. L. Yao, ASME J. Manuf. Sci. Eng. **124**, 369 (2000).
[3]L. A. Hackel, Light Met. Age, **30** (December 2003)
[4]L. A. Hackel and F. B. Harris, U.S. Patent No. 6410884 (June 25, 2002).
[5]M. Zhou, Y. Zhang, and L. Cai, J. Appl. Phys. **91**, 5501 (2002).
[6]M. Zhou, Y. K. Zhang, and L. Cai, Mater. Sci. Forum **77**, 549 (2003).
[7]M. Geiger, M. Kleiner, R. Eckstein, N. Tiesler, and U. Engel, CIRP Ann. **50**, 445 (2001).
[8]J. Cao, N. Krishnan, Z. Wang, H. Lu, W. K. Liu, and A. Swanson, ASME J. Manuf. Sci. Eng. **126**, 642 (2004).
[9]M. Otsu, T. Wada, and K. Osakada, CIRP Ann. **50**, 141 (2001).
[10]G. Esser, M. Schemidt, and M. Dirscherl, Proc. SPIE **5063**, 177 (2003).
[11]Y. Wang, Y. Fan, S. Vukelic, and Y. L. Yao, J. Manuf. Process. **9**, 1 (2007).
[12]J. R. Rice, Mech. Mater. **6**, 317 (1987).
[13]H. Chen, Y. L. Yao, and J. W. Kysar, ASME J. Manuf. Sci. Eng. **126**, 226 (2004).
[14]R. J. Asaro, Adv. Appl. Mech. **23**, 1 (1983).
[15]Y. Huang, Division of Applied Sciences, Harvard University, Report No. 178, 1991 (unpublished).
[16]J. W. Kysar, Division of Engineering and Applied Sciences, Harvard University, Report No. 178, 1997 (unpublished).
[17]W. Zhang and Y. L. Yao, J. Manuf. Process. **3**, 128 (2001).
[18]J. W. Hutchinson, J. Mech. Phys. Solids **16**, 13 (1968).
[19]P. Connolly and P. McHugh, Fatigue Fract. Eng. Mater. Struct. **22**, 77 (1999).
[20]J. W. Kysar, J. Mech. Phys. Solids **49**, 1099 (2001).
[21]D. Peirce, R. Asaro, and A. Needleman, Acta Metall. **31**, 1951 (1983).
[22]P. Savage, B. P. O. Donnell, P. E. McHugh, B. Murphy, and D. Quinn, Ann. Biomed. Eng. **32**, 202 (2004).
[23]L. W. Meyer, *Shock-wave and High-Strain-Rate Phenomena in Metals* (Dekker, New York, 1992), pp. 49–68.
[24]D. V. Wilson, J. Phys. D **7**, 954 (1974).
[25]H. Chen, J. W. Kysar, and Y. L. Yao, J. Appl. Mech. **71**, 713 (2004).
[26]J. R. Rice, J. Mech. Phys. Solids **21**, 63 (1973).
[27]Y. Wang, J. W. Kysar, and Y. L. Yao, Mech. Mater. **40**, 100 (2006).
[28]J. R. Booker and E. H. Davis, J. Mech. Phys. Solids **20**, 239 (1972).